

doi: 10.18720/MCE.69.1

Modeling of porous material fracture

Моделирование разрушения пористого материала

A.N. Levandovskiy,

B.E. Melnikov,

Peter the Great St. Petersburg Polytechnic University, St. Petersburg, Russia

A.A. Shamkin,

Corning SNG OOO, St. Petersburg, Russia

Младший науч. сотрудник

А.Н. Левандовский,

д-р техн. наук, профессор Б.Е. Мельников,

Санкт-Петербургский политехнический университет Петра Великого, г. Санкт-Петербург, Россия

научный сотрудник А.А. Шамкин,

ООО «Корнинг СНГ», г. Санкт-Петербург, Россия

Key words: porous material; fracture; tomography; element deletion; element erosion; element size; fracture criterion; finite element; cordierite; cubic elements

Ключевые слова: пористый материал; разрушение; томография; удаление элементов; разрушение элементов; размер элемента; критерий разрушения; конечный элемент; кордиерит; кубические элементы

Abstract. Wide use of various porous materials in construction engineering applications requires development of up to date methods of non-destructive characterization and optimization of such materials. This work explores an approach to modeling of fracture of a brittle porous material. Available 3D digital data on the specimen geometry is converted into uniform finite element mesh consisting purely of elements of cubic shape. Fracture model is based on a series of linear solutions. Thus approach to linear modeling described in the previous papers could be utilized. Fracture is modeled by consecutive element erosion. A special element erosion criterion is established to avoid finite element size dependency. Two speed-up algorithms are proposed and tested. The approach described can be used for modeling fracture of uniform construction materials, also materials with inclusions under various mechanical and thermal loads.

Аннотация. Использование пористых материалов в промышленном строительстве требует разработки современных неразрушающих алгоритмов исследования и оптимизации эффективных механических свойств этих материалов. В настоящей работе рассмотрен подход к моделированию разрушения пористых материалов. Доступная трехмерная цифровая информация о структуре конвертируется в конечно-элементную модель, состоящую исключительно из одинаковых элементов кубической формы. Модель разрушения базируется на последовательности решений линейных задач. Таким образом, модели, разработанные ранее для моделирования линейных задач, могут обоснованно использоваться. Разрушение моделируется последовательным удалением элементов. Используется специальный критерий разрушения для удаления конечных элементов, который позволяет нивелировать сеточную зависимость. Так же предложены алгоритмы ускорения моделирования разрушения. Описываемый подход может использоваться для моделирования однородных строительных материалов, а так же материалов с включениями под воздействием различных температурно-механических нагрузок.

Introduction

Porous structures based on brittle matrices are widely used in building construction and other engineering applications. The key ones to be mentioned: industrial ceramics including chemical- and corrosion-resistant materials, acid-proof wares, decorative tiles, refractory materials and products, bricks, road bricks, blown-out concrete, claydite and other fillers for light concrete, roof tiles, crucibles, troughs, molds for metal, glass, oxide fusion and forming, membranes and filters for mechanical and chemical (catalytic) liquid and gas cleaning [1–2], lined pipes, diesel and gasoline discharge gas filters, electronic high-temperature applications, bio-medical ceramics, domestic ceramics, sanitary earthenware [36].

The use of porous materials in modern civil engineering requires development of up-to-date methods and algorithms for non-destructive analysis of such materials and their thermo-mechanical property prediction.

Mechanical properties of porous materials were studied analytically, numerically and experimentally, at the most novel experimental facilities.

In the middle of the 20th century Gassmann developed equations, establishing a connection between the elastic parameters of porous matter, filled with liquid or gas [3]. Gassmann's equations are used in geo-physics to estimate effective elastic properties of rocks.

During the last decades a number of papers were published, containing theoretical as well as half-empirical manipulations on the effective linear properties of the porous structures of the specific kinds [4–9].

Numerical studies of the effective properties of the multi-phase and porous structures are conducted namely with the use of finite element method (FEM). The idea of FEM was originally formulated more than 50 years ago [10]. A considerable contribution to the development of FEM was made by the Russian scientists and representatives of the St. Petersburg Polytechnic school [11–14].

Calculations on representative specimens of 3D non-periodic porous structures require a substantial amount of computer memory (of the order of tens of gigabytes). Therefore in most published papers authors only deal with periodic geometry structures, artificially generated (not existing in nature) on a computer with the use of some random algorithms [7, 15–20].

Only during the past years it became possible to directly simulate porous 3D structures. The problem had not been only with the computer power but also with the devices capable of digitizing the whole depth of the structures (not just surfaces) with extremely high resolution: median pore size in some could be as small as just a few microns. The first method to be mentioned here is the computer micro tomography [21]. With the use of tomography data the numerical studies of the microstructures are conducted [22–27]. Primarily those studies deal with bone properties. Some geological research may also be referred to [28].

The present investigation is based on the approaches to porous structure linear modeling described by the authors in the earlier papers [24]. The fracture models established here consist of series of linear runs similar to the ones used earlier to calculate the effective elasticity and thermal conductivity [24].

In [22, 23, 29, 30] attempts are made to simulate 2D material structures based on electronic microscopy and spectroscopy data.

Rarely is any special attention paid to the tomogram resolution and mesh convergence [17, 18, 24].

Besides traditional macroscopic experimental studies of the mechanical parameters of the porous structures [31, 32] for microstructure study special methods are developed and applied. The most useful of those is probably the neutron diffraction method to study deformation of the structures at micro-level [33–35, 7, 24, 37]. In the present study as an example of such methods tomography data is used.

The aim of the current research is to develop a method of modeling fracture of a porous material when the material geometry is taken from 3D tomography images. The method should be invariant to the finite element (FE) mesh used. Since FE models used consist of identical FE of the cubic shape and the locations of the FE elements are prescribed (mesh could not be skewed etc.), there is only one important task that needs to be solved: the fracture model should give identical or convergent results on meshes with different FE sizes (e.g. meshes based on different tomography resolutions).

The modeling approach could then be used to model fracture of various porous construction materials or materials with inclusions, under mechanical and thermal loads.

Fracture is modeled under external uniaxial tension and compression by element deletion technique. The incrementally deleted (finite) elements approximately trace the crack initiation and propagation over the structure. Respective degradation of elasticity of the cracked body is evaluated at each step and so calculated stress-strain curves provide comprehensive information on effective Young's moduli, fracture toughness, tensile/compressive strength, and strain tolerance. The key of the simulation approach is the criterion for element deletion that delivers physically meaningful stress-strain curves with the results being stable at different finite element sizes (tomography resolutions).

Methods and materials

Material structures are presented by 3D arrays of solid cubic elements (voxels) of isotropic matter.

The following three types of materials are considered:

1. Virtual overlapped spherical pores structures of $100 \times 100 \times 100 = 10^6$ voxels and total porosity of 0.3, 0.4, 0.5, and 0.6 (Figure 1)

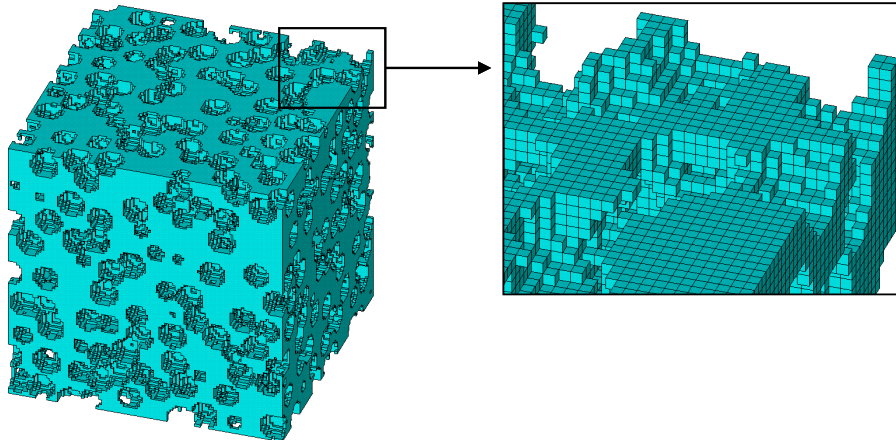


**Figure 1. FE model of a virtual structure of overlapped spherical pores.
Porosity = 0.5**

2. Virtual overlapped spherical solids structures of $100 \times 100 \times 100 = 10^6$ voxels and total porosity of 0.41, 0.52, and 0.63 (Figure 2). These structures have been obtained by inverting overlapped spherical pore structures. The procedure of inversion assumed “dust removal” for correct porosity evaluation, i.e. deleting the solid element cluster not connected to the main body that has originated from isolated pores inversion.

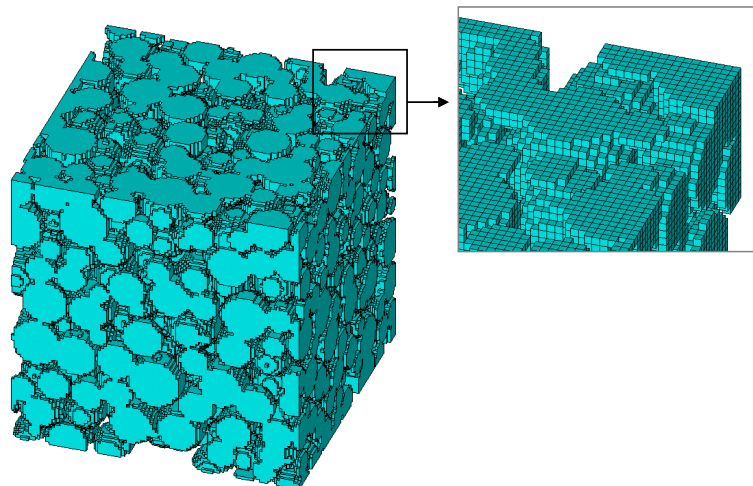


**Figure 2. FE model of a virtual structure of overlapped solid spheres.
Porosity = 0.5**

3. 3D tomography samples of real materials. R1 and A1 (Figure 3).

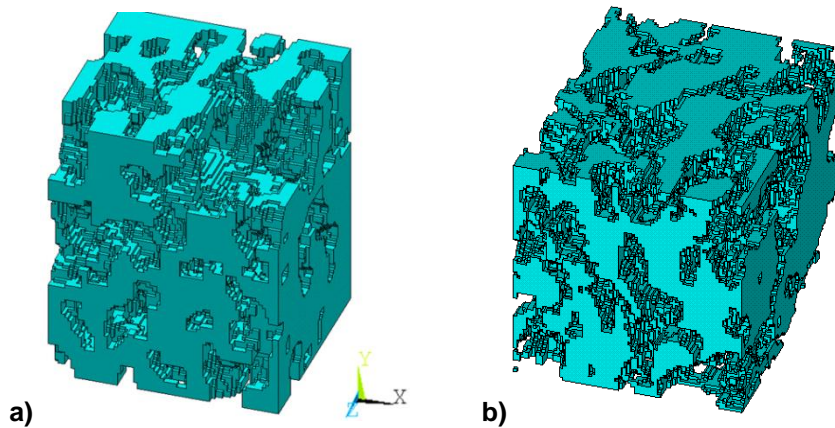


Figure 3. FE models of a quarter of sample R1 (a) and the whole sample A1 (b)

Earlier papers are referenced here to give more details on the 3D FE models based on tomography data [24, 25, 37].

Figure 4 [7] shows the statement used to calculate stress-strain response of the specimens at the macro-level. Out of a number of statements possible [38] the displacement BCs are used to be able to track material response after maximum stress is reached.

Specimen fracture is simulated by element deletion (erosion) approach: a structure is loaded until the critical value of the chosen criterion in a FE is reached. The criterion value in a FE is determined by averaging over all 8 nodes of the element. One linear task could be solved at any load and then scaled accordingly (Figure 5). Afterwards the element is removed and so on. In most simulations here an arbitrary trial value is taken for the critical criterion value for comparative analysis purposes. All tasks appear to be essentially linear. So all calculated stress-strain dependencies could be linearly scaled for any other critical criterion value. The absolute critical value for the criterion could be estimated once an experimental data set is available to fit the modeling data to.

ϵ^1 – the first principal strain norm is used in most simulations as a criterion typical for brittle materials. σ^1 – the first principal stress could also be applied.

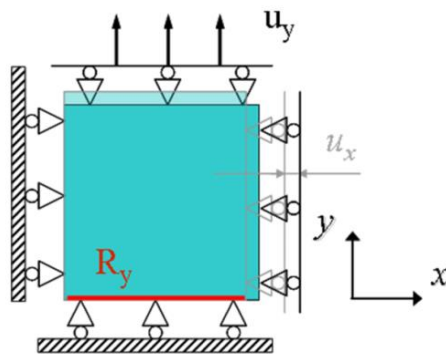


Figure 4. BCs used in the simulations (displacement is applied, reaction force is measured) to calculate stress-strain response of the specimens [7]

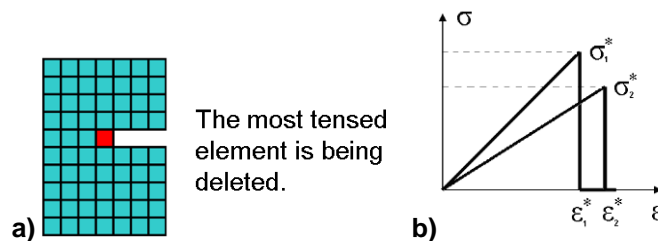


Figure 5. a) One step for crack propagation calculation

b) Input properties of elements for different materials (1) and (2)

Numerical values of input parameters and their meanings will be noted in line with calculated results by specific material number from Table 1 below. Here the following notations are used:

ε^*_{crit} – critical value of first principal strain, at reaching which the element needs to be deleted,

γ – surface cleavage energy, corresponding to the critical value of the criterion, calculated from (4).

Table 1. Properties of the considered materials

Material	ε^*_{crit} , %	E, GPa	γ , J/m ²	Element size, μm
1	1.71	340	25	1.0
2	1.40	340	25	1.5
3	0.99	340	25	3
4	1.62	340	25	1.12
5	1.48	340	25	1.34
6	1.32	340	25	1.68
7	1.15	340	25	2.24
8	0.936	340	25	3.36
9	0.662	340	25	6.72
10	0.752	340	25	5.2
11	1.21	340	25	2
12	16.7	144	-	-

Results

Crack initiation points

The effect of external load in R1 structure is simulated as shown in Figure 4. The elements exceeding a certain strain could be selected, as shown in Figure 6, where “y” – vertical axis, “micro” and “macro” relate to values averaged over one FE or effectively over the whole structure. The probability density of the elementwise 1st principal strain distribution normalized by macroscopic (effective) uniaxial strain is shown in Figure 6 together with the picture showing space distribution of the most tensed elements. One can see that the elements are not concentrated in one location, they are rather randomly distributed through the volume, which means that we should expect multiple crack initiations and development in many locations simultaneously rather than a single crack propagation phenomena.

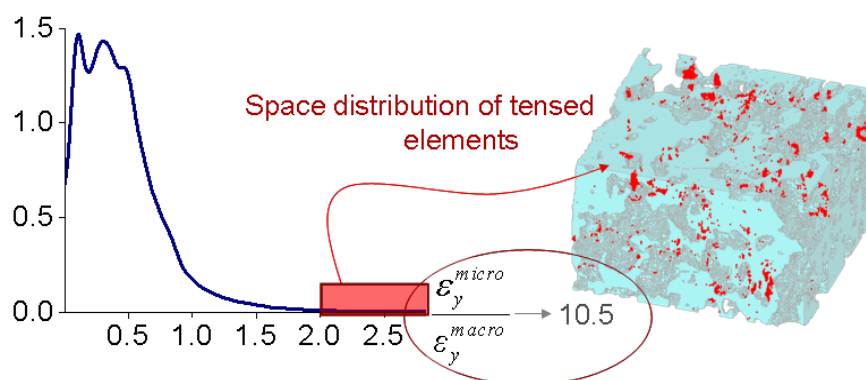


Figure 6. Strain probability distribution (left) and Space distribution of the most tensed elements in terms of the 1st principal strain value (right) for R1. Since critical points are not concentrated, a single crack development would not occur; rather a lot of small sub-cracks can be expected

Number of elements to be deleted at each iteration

An attempt is made to speed up the solution. At first the number elements to be deleted at one step is estimated. The accurate way of fracture calculation is to delete the most stressed elements one by one and recalculating the strain distribution after each step. Calculations can be significantly increased if the number of elements being deleted at each step is more than one.

The diagram in Figure 7 illustrates a comparison of two stress-strain curves evaluated on the same tomogram, a quarter of R1, with one and eight elements being deleted at one step. On the plot “y” denotes the axis of loading, “macro” – values recalculated from the BC and the effective reactions on the borders, ϵ^{*iso} – the critical value for the first principal strain element erosion criterion (see material #12 from Table 1).

In this particular case the curve difference looks negligible so the calculation speed up could be more valuable than accuracy.

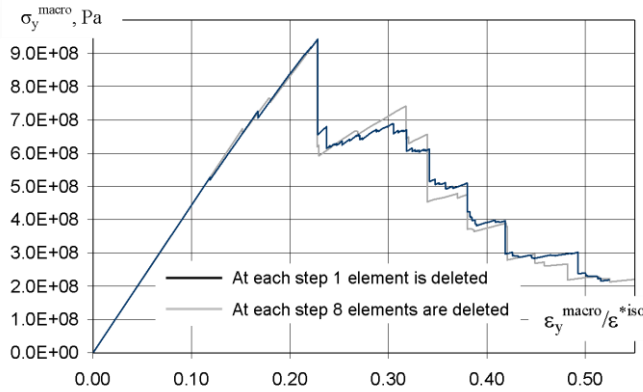


Figure 7. Tensile stress-strain curves for a quarter of R1 specimen (85 x 70 x 65 voxels, 85 x 70 x 65 elements) with different number of elements deleted at one step. Material # 12

Interestingly the deletion of elements begins at the strain level of approximately ten times less than the element strain tolerance. That implies high non-uniformity of micro strain/stress distribution in the pore structure.

Another alternative way to potentially speed up the process is to use a number of load steps. If the value of maximum load that the specimen can bare is approximately known, one could take a portion of that load and check if any of the FEs need to be deleted (using an element fracture criterion). When those elements are removed, another linear iteration is run with the load unchanged. The process repeats until there are zero elements to remove. Afterwards the next portion of the load is added and so on. The plot below (Figure 8) illustrates the quality of the results obtained with different speed-up techniques on the A1 tomography specimen. It is clearly seen from Figure 8 that one can obtain reasonably good stress-strain results spending less than 6% of the time needed for an “ideal” solution (1 deleted element per each linear solution). The most beneficial technology is the stepped load version of the algorithm.

Most of the results in the following paragraphs are obtained deleting 3 elements at each linear calculation iteration. The stepped load approach is not used in for the simulations described in this paper because historically it was developed later in particular for thermal fracture simulations.

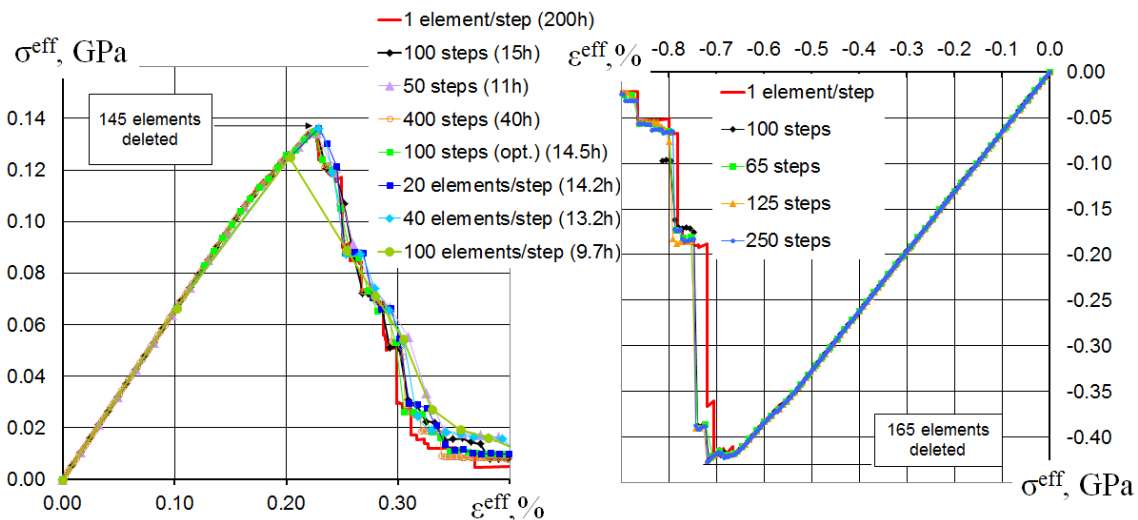


Figure 8. Tensile stress-strain curves for the A1 specimen (E = 340 GPa, FE size is 5.2 μm), “x” direction. “Eff” denotes effective quantities.

Stress-strain dependency for spherical pores/solids structures

In this section the results of fracture simulation with selected 1st principal strain criterion are shown for virtually generated structures. Simulated resolution (element size) is 1 micron at median pore size $d_{50} = 5.5$ microns. The structures with spherical pores have pore morphology parameter [24] $m \sim 2$, the 1st principal strain criterion assumed with the material properties corresponding to Material # 12 from Table 1.

Structure compressive and tensile strength both decrease with porosity and pore morphology factor (m). Tension always breaks the sample into two parts, whereas compression can produce more parts (Figures 9–12).

The ratio of tensile strength to compressive strength is about 3 at $m = 2$ (Figure 13) and tends to lower to the value of 2.4 at higher pore morphology $m = 4.24$ (Figure 14, see also table 5 at the end of the section).

Tensional strain tolerance (strain corresponding to the effective strength of the structure) increases with porosity at a constant m value and also increases with m at a constant porosity (Figure 13–14).

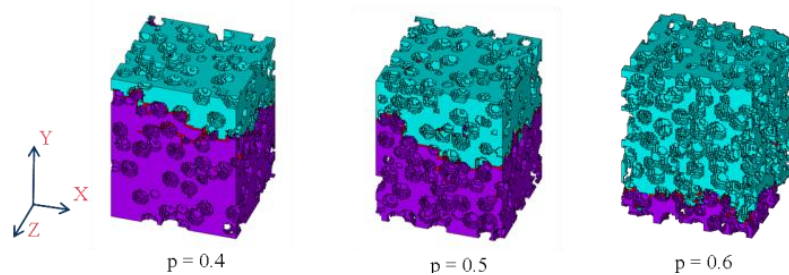


Figure 9. Overlapping spherical pores. Tension

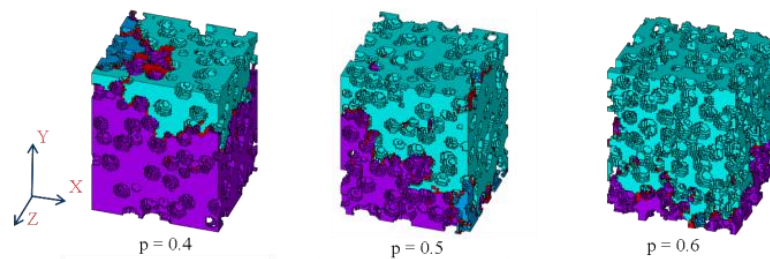


Figure 10. Overlapping spherical pores. Compression

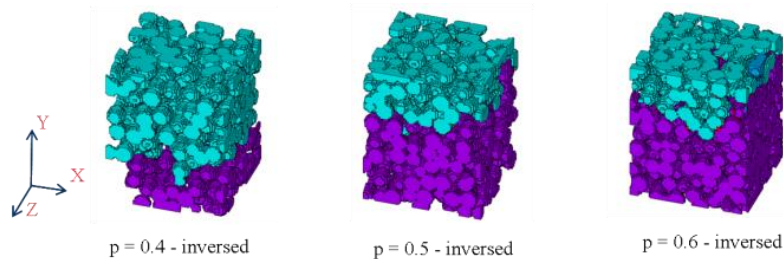


Figure 11. Overlapping spherical solids. Tension

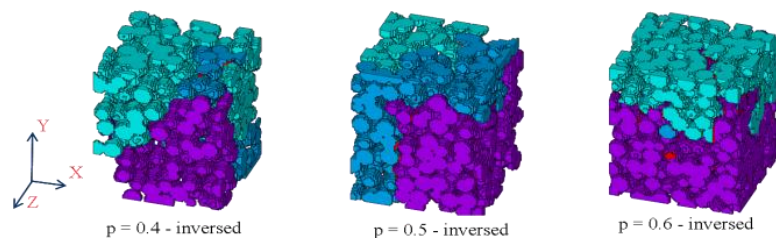


Figure 12. Overlapping spherical solids. Compression

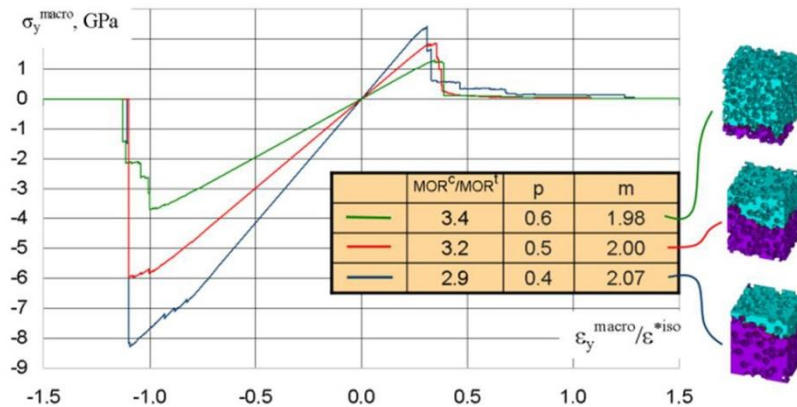


Figure 13. Overlapping spherical pores. Stress-strain curves. Material #12

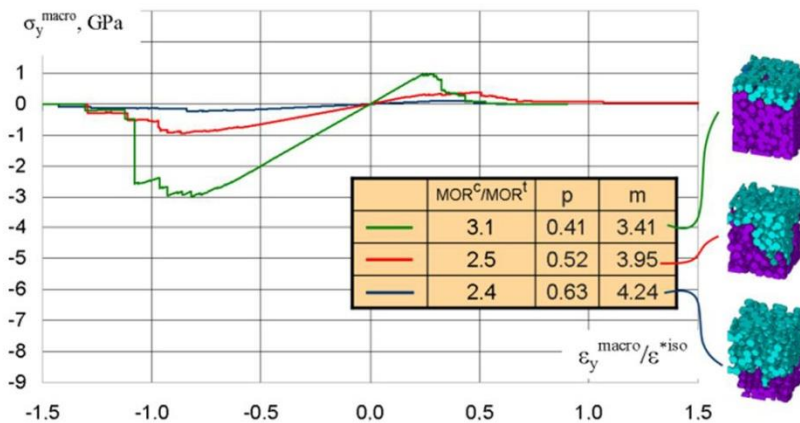


Figure 14. Overlapping spherical solids. Stress-strain curves. Material #12

Influence of extrusion process

As far as tensional strain tolerance increases with p , one can conclude that it is generally beneficial to use high-porosity materials in the applications where large thermal gradients exist, like exhaust filters.

It is also important the tensional strain tolerance increases with m . As shown in [39–40], filter walls are weaker in the directions perpendicular to the extrusion axis. Taking into account that these are the directions of the highest thermal gradients [41–42] the following conclusion is formulated: extrusion process itself has a positive influence on the overall thermal shock resistance of the filter structure. A solid statistical confirmation of this conclusion is a subject of future studies.

Element erosion criterion modifications to be used at different FE sizes

While simulating fracture of another part of R1 - 120³ piece (taken cube 120x120x120 1um voxels, and then coarsened to 6 um voxels) with 1st principal strain criterion at various element sizes, an approximately square root dependency of calculated MOR (maximum stress, effective strength of the specimens) on element size has been observed (Figure 15–17).

In Figure 15 the plots calculated for the same material structure and solid element properties (material #12) but different element sizes are shown. It can be seen that all the plots have similar shape but the scale is different. This is caused by the fact that element stresses/strains depend on the element size. For example element stresses and strains may reach infinite values (due to presence of re-entrant angles) if we take a zero volume of averaging – zero element size. The larger element size we take, the less the value of maximum element stresses/strains in the structure we have. So for larger elements we will have to apply larger macroscopic tension for the tensed elements to fail.

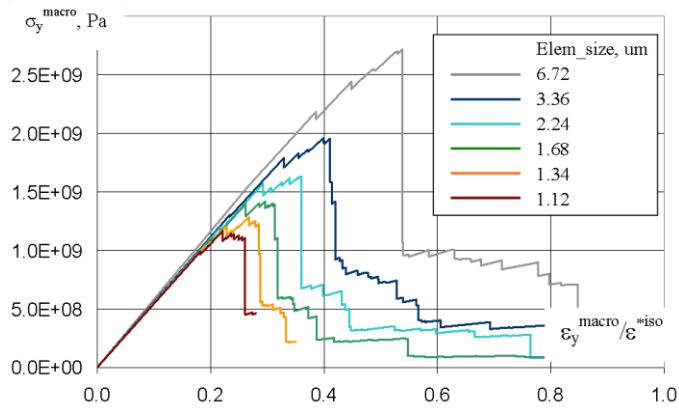


Figure 15. Stress-strain calculation dependence on cubic element size. Simple, element size independent, maximum strain criterion. Material #12

To exclude the dependency on FE size, the following modification of element failure criterion has been developed

As it is known from the general elasticity theory, in the field of macroscopic stresses in the vertices of the re-entrant corner there stresses and strains are not regular and tend to infinity [43]. In the vicinity of a vertex strain and stress tensor component are inversely proportional to the distance to the vertex r in a power λ :

$$\begin{aligned} \varepsilon_{ij} &\sim \frac{1}{r^\lambda} \\ \sigma_{ij} &\sim \frac{1}{r^\lambda} \end{aligned} \tag{1}$$

For the exponent λ there is some theoretical data:

- in a crack tip it is equal to 0.5 [43];
- in a right corner tip it is 0.455 [43].

λ or $\langle \lambda \rangle$ is not easy to determine in our cases since FE models are of finite sizes and the type of defect vary for each stressed element.

It is proposed to check the 1st principal strain distribution in the elements that were deleted during fracture simulation of R1 quarter (Figure 15). For each FE 1st principal strain is scaled such that macroscopic strain on the specimen is constant (1% in this particular case). Then the median first principal strain is taken for each FE size (averaged among all deleted elements) and put on a plot (Figure 16). After power interpolation along the points on the plot (Figure 16) $\langle \lambda \rangle$ is obtained for the current structure.

In the Table 2 the results are given for median $\langle \varepsilon^1 \rangle$ and $\langle \lambda \rangle$ for the structures studied. All values are in the range 0.455–0.497.

Table 2. Median average values for ε^1 and λ for the structures studied

	Tension	Compression
R1 (120 ³ sample)	$\langle \lambda \rangle = 0.477$	$\langle \lambda \rangle = 0.455$
$r, \mu\text{m}$	$\langle \varepsilon^1 \rangle$	$\langle \varepsilon^1 \rangle$
6.72	$2.03 \cdot 10^{-2}$	$7.87 \cdot 10^{-3}$
3.36	$2.65 \cdot 10^{-2}$	$1.05 \cdot 10^{-2}$
2.24	$3.10 \cdot 10^{-2}$	$1.27 \cdot 10^{-2}$
1.68	$3.60 \cdot 10^{-2}$	$1.42 \cdot 10^{-2}$
1.34	$4.03 \cdot 10^{-2}$	$1.62 \cdot 10^{-2}$
1.12	$4.60 \cdot 10^{-2}$	$1.80 \cdot 10^{-2}$
R1 (quarter sample)	$\langle \lambda \rangle = 0.497$	$\langle \lambda \rangle = 0.462$
$r, \mu\text{m}$	$\langle \varepsilon^1 \rangle$	$\langle \varepsilon^1 \rangle$
6.72	$2.72 \cdot 10^{-2}$	$9.59 \cdot 10^{-3}$
3.36	$3.91 \cdot 10^{-2}$	$1.41 \cdot 10^{-2}$
2.24	$4.68 \cdot 10^{-2}$	$1.57 \cdot 10^{-2}$

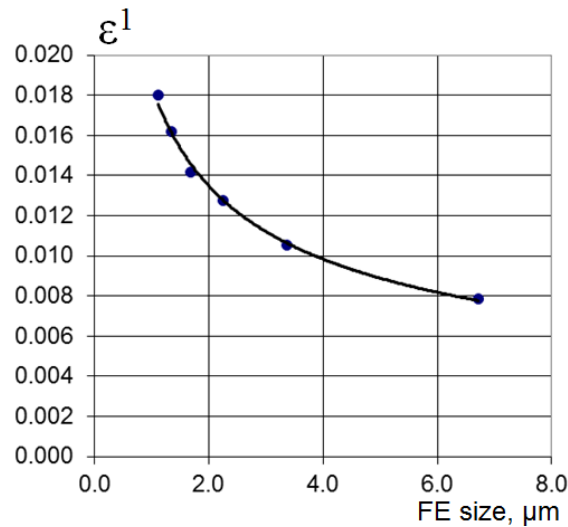


Figure 16. Median average values of ϵ^1 in the deleted elements in the special task described in the text. Specimen R1 120x120x120. Compression. $\langle \lambda \rangle$ calculated is 0.455

Taking into account what is said above about $\sigma(\epsilon)$ scaling on different meshes with the constant criterion $\epsilon^1 = \epsilon^*$, a modified element erosion criterion is introduced, that depends on the FE size as follows:

$$\begin{aligned} \epsilon^1 &= \epsilon^*(r), \\ \epsilon^*(r) &= \epsilon^*(r_0) \left(\frac{r_0}{r} \right)^\lambda, \\ \epsilon^*(r_0) &= \epsilon_0^*, \end{aligned} \quad (2)$$

where r – FE element edge length;

r_0 – base FE element edge length, for which critical ϵ_0^* is assumed to be known;

λ – average power exponent (singular exponent), determined by the geometry and BC.

$\lambda = 0.5$ is suggested for simplicity and only small potential inaccuracy for very different FE sizes ($\frac{1}{\sqrt{\lambda}}$ varies by no more than 10 % at even 10 times changes of r – FE element edge length).

Test simulation results below (Figure 17–20) show that the modified criterion of element fracture yields comparable and converging results at different meshes.

The value of ϵ_0^* could be determined if suitable experimental data is available. The data could be either a macro stress-strain dependency for tension or compression of a specimen of a known material (material for which typical geometry information is available, e.g. through 3D tomography). Then a trial FE simulation based on the known geometry (with ϵ_0^* of an arbitrary choice) is compared against the experimental data. Based on that comparison the value of ϵ_0^* is chosen that provides the best fit of the experimental data.

Another option could be used when fracture of a thermally microcracked material [37] is simulated. Such materials consist of orthotropic domains and are intact (have no cracks) at some reference temperature (typically around 1200 °C). The material structure and thermally induced microcracking upon cooling could be simulated. If effective Young's modulus on temperature dependency $E^{eff}(T)$ for the material is known then it could be compared to the simulation results. Based on that comparison the value of ϵ_0^* is chosen that provides the best fit of the experimental data.

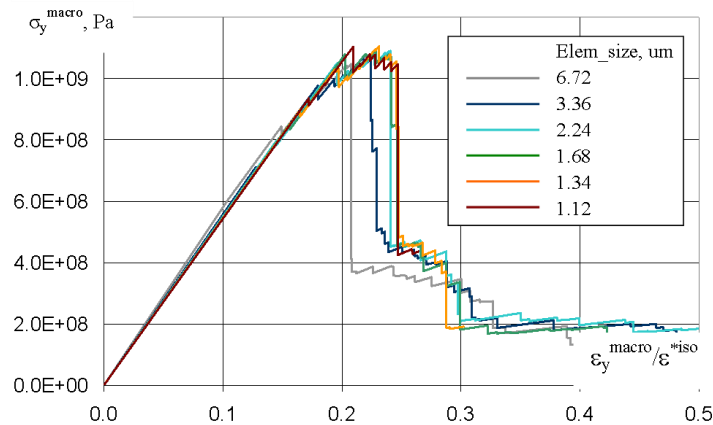


Figure 17. Stress strain curve. Critical criterion value scaled as the square root of element size (2), (4)

Another explanation to the criterion modification for different FE sizes could be suggested.

Based on Griffith's theory we state here that element fails when energy of tension reaches the energy of crack surface development and present the event by the energy balance equation as follows

$$\frac{1}{2} E \cdot \varepsilon^* \cdot \sigma^* \cdot d^3 = 2 \gamma \cdot d^2 \quad (3)$$

where d – element size, E -Young's module, ε^* - strain of element fracture, σ^* - stress of element fracture, γ - surface (cleavage) energy, are the properties of cubic element.

The critical values are given by:

$$\varepsilon^* = \sqrt{\frac{4\gamma}{E \cdot d}} \quad (4)$$

In the formulas above factor "2" (3, right side) is due to the fact that when a crack develops typically 2 free surfaces are created. Ideally speaking in our case there should be come variable between 1 and 4, corresponding to the amount of free surface created when a FE is deleted. Also ε and σ should be considered to be tensors and their scalar product will be a scalar, inversely proportional to so some power of d (element size). The power will be the same for all tensor components. Then anyway this power will be obtained from (4) and will be equal to 0.5.

One can see that new element failure criterion (scaled element failure criterion or "Gamma criterion") for stress-strain simulation depends on square root of element size. This criterion is expected to provide consistent results at similar meshes with different element size.

We found in the previous research [24] that solid element size for accurate estimation of Young's modulus and fluidic permeability of pore structures should be less than median pore size d_{50} . The developed Gamma criterion would bring an additional condition related to correct strength estimation, namely determining the critical element size for accurate evaluation of the both elasticity and fracture. We will test the criterion in a range of element sizes and determine the ranges of criterion validity regarding pore size, porosity, and pore morphology.

FE size for R1 sample

A precise look on images of crushed sample (Figures 18-19), a quarter of R1 (85 x 70 x 65 voxels, 85 x 70 x 65 elements), and relative stress-strain curves (Figure 20) with element sizes $d = 2.24$ -6.72 microns (but the same geometry corresponding to voxel size of 6.72 microns) at pore size $d_{50} = 20$ micron (material # = 7, 9 respectively) has shown that tension breaks a porous sample into two pieces (Figure 18) and looks very similar for all element sizes. However one can see more branching cracks for fine elements than for coarse elements (Figure 18).

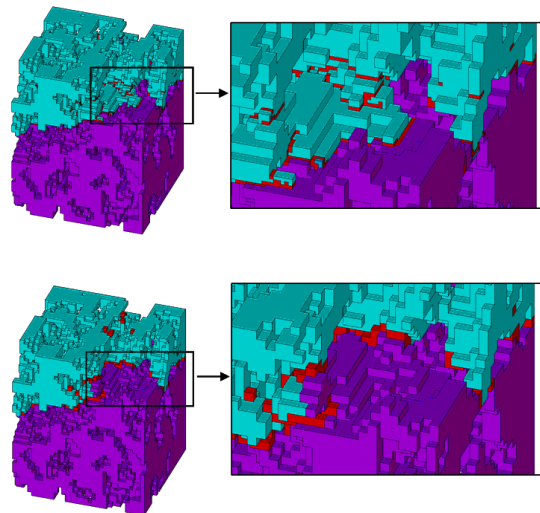


Figure 18. R1. Tension. Different element sizes (top-2um, bottom-6 um) used on the same geometry

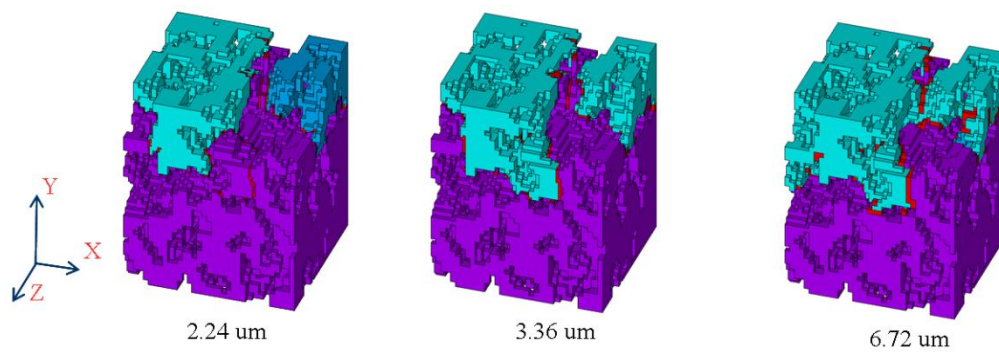


Figure 19. R1. Different element sizes used on the same geometry. Compression

The stress-strain plots for the structure are very similar to each other as well and the tensile strength obtained with the gamma criterion is the same essentially for all element sizes (Figures 20–21).

Compression test shows three pieces for small elements and two parts for coarse elements (Figure 19). Crack path variation on element size is higher at compression than at tension. However all three predicted compressive strength values are very consistent, and a nearly identical match is observed for material # 7 and 8.

The data has shown that results of strength estimation coincide for element sizes less than half of mid pore size.

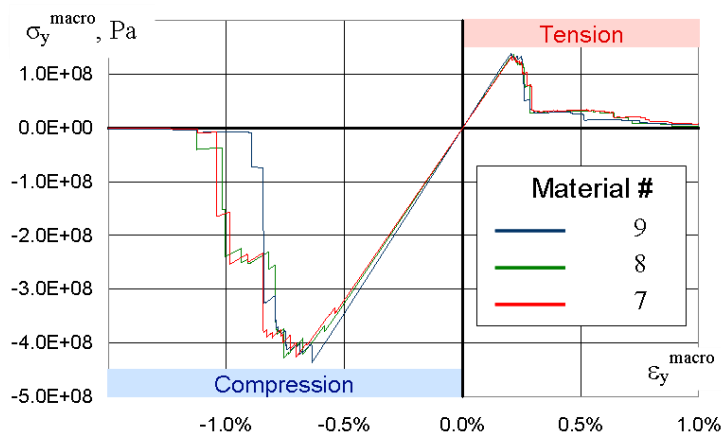


Figure 20. R1. Different element sizes used on the same geometry. Stress-strain curves

A larger sub-sample of R1 – 120^3 piece (taken cube $120 \times 120 \times 120$ 1 μm original voxels, but then coarsened to 6 μm voxels) - was chosen to investigate the stress-strain curves dependence on a wider range of element sizes. Again in this test (simulated coarsened) pore geometry does not change, gamma criterion is used, alumina properties are taken as solid matter input: $E = 340 \text{ GPa}$, $\nu = 0.23$, $\gamma = 25 \text{ J/m}^2$

The plot from figure 21 shows the results of the calculations. Important fact is that the curves for finer elements are closer than for coarse mesh, which means we have “mesh convergence”. The calculations have confirmed that Material # 7 (element size 2.24 microns) and lower provide very consistent estimations of tensile strength and strain tolerance and good estimations for compressive values.

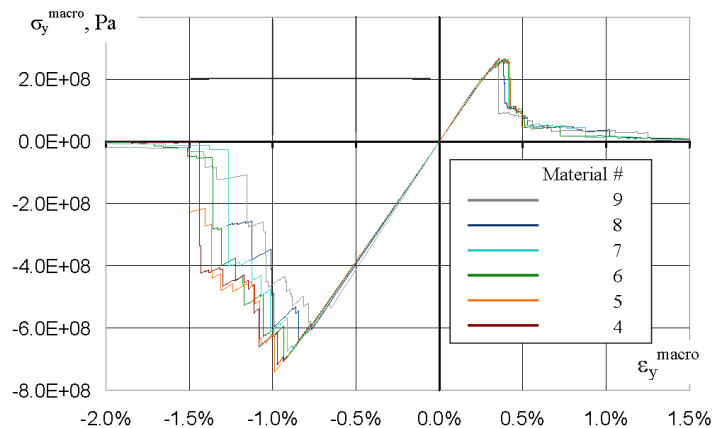


Figure 21. Stress-strain curves for R1 120^3 – good match for tensile strength. For compression, curves look similar with some offset. The curves for finer elements are closer to each other, than for coarse mesh – “mesh convergence”

FE size for overlapping spherical pore/solid structures

For overlapping pore structures (simulated pore size 5.5 micron, voxel 1 μm) the stress-strain curves have been obtained with gamma criterion on various porosities between 0.3–0.6. Alumina properties assumed are $E = 340 \text{ GPa}$, $\nu = 0.23$, $\gamma = 25 \text{ J/m}^2$, element size = voxel size = 1 μm , $\epsilon^* = 1.71 \%$.

For the structure with 0.3 porosity, coarser resolution of 2 μm was simulated as well. The difference of calculated MORs is 10 % for compression and 9 % for tension (Figure 22).

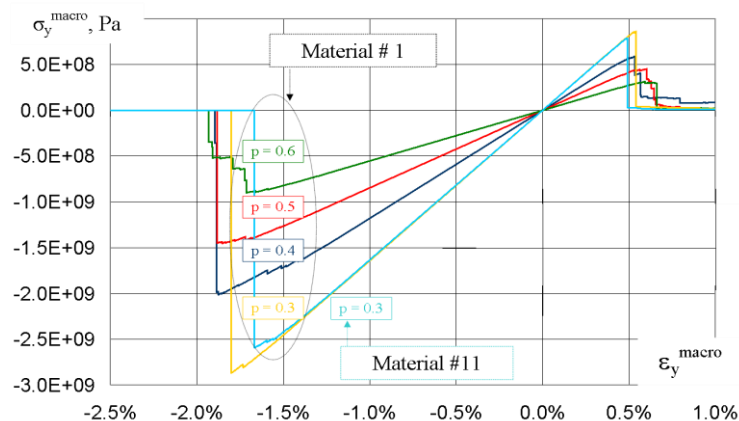


Figure 22. Virtual structures with different porosities. For $p = 0.3$ the calculations are also done with simulated coarser resolution – one voxel = 2 μm with element size of 2 μm

The following plot (Figure 23) shows the comparison between the above curves (Figure 22, shown in shadow in Figure 23) and another set of calculated curves for larger pieces of the virtual structures (100^3 vs 80^3) for porosities of 0.4, 0.5 and 0.6 (top-down respectively). The element sizes are 3, 1.5 and 1 μm (top-down respectively). Voxel size is 3 μm .

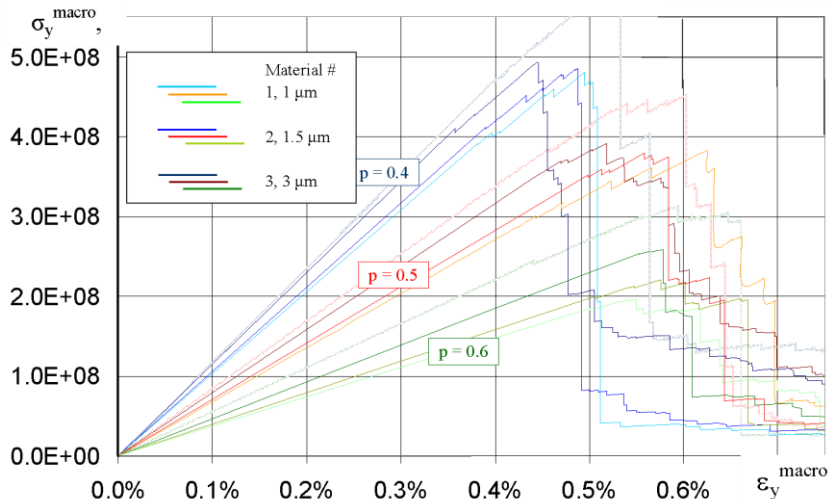


Figure 23 Spherical pore structures with various porosities. Stress-strain curves for tension

Tables 5 and 6 and Figures 24, 25 show the results of the numerical experiments described above. One can observe that MOR values calculated with different element sizes for each structure fall in 10 % for tension and 20 % for compression except 35 % in case of overlapping spherical pores at $p = 0.6$. The difference between two neighboring values is lower than 10 % in all cases except 25 % in case of overlapping spherical pores at $p = 0.6$. The larger difference for $p = 0.6$ can be attributed to the fact that we have thinner walls between the pores in this case and more elements are needed per each wall.

Based on the comparison of 100 micron and 80 micron size sample simulation results (shadowed and solid lines in Fig. 23), one can conclude that at the size of 100 micron and above the effective Young's moduli are not going to experience any significant change. In other words samples of overlapping spherical pores and conversely overlapping spherical solids (as far as both could be considered a mutual inversion) are representative when their linear dimensions are 8-10 larger than their median pore size d_{50} . Presumably natural structures with irregularly shaped pores should require larger sample size to produce stable mechanical property calculation/experimental results.

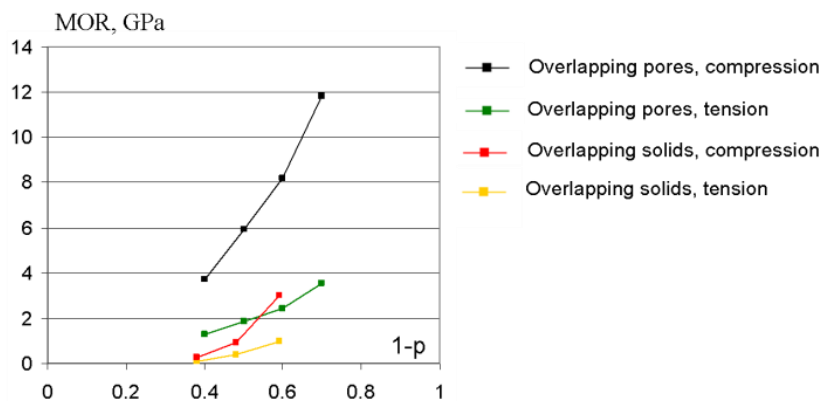


Figure 24. Strength of spherical pore and spherical solids structures with various porosities under tension and compression

A few series of simulations on structures with the same voxel and element sizes were carried out to develop insight into a model of strength dependence on pore structure. We have simulated four overlapping spherical pore structures with voxel size of 1 μm and element size 1 μm and also three structures of overlapping solid spheres all with structure voxel size of 1 μm , element size 1 μm and input of material properties #12 (see Tables 3–6).

The obtained data show steady non-linear dependence of calculated strength on porosity.

It was found that the strength is proportional to factor $(1-p)^m$ in each data series with a standard deviation about 4 % for compression and 10 % for tension (see Table 6).

Based on the preliminary model interpretation, calculated strength dependence on porosity and pore morphology is given by

Levandovskiy A.N., Melnikov B.E., Shamkin A.A. Modeling of porous material fracture. *Magazine of Civil Engineering*. 2017. No. 1. Pp. 3–22. doi: 10.18720/MCE.69.1

$$Strength(p,m) = S_0 \cdot (1 - p)^m \quad (5)$$

Interestingly the strength model obtained here has the same dependence on p and m as the dependence for Young's modulus.

The value of the S_0 parameter in equation (5) has a physical sense of the strength at zero porosity. It is known to depend on grain size and material tensile strength. Presumably the S_0 value simulated in tension must be equal to the value $\sigma^* = E \cdot \epsilon^* = 24$ GPa. It is not quite the case here. The parameter calculated as $S_0 = Strength / (1-p)^m$ stays constant versus porosity within one data set for a specific structure. However a difference is observed between the data sets, which needs physical interpretation in future.

Whereas the average values in Tables 3-5 look similar for different structures as compared separately at tension or at compression, the compressive values are about three times higher than the respective tensile values. The ratio slowly decreases with m as demonstrated at Figure 25.

Table 3. MOR and strain tolerance at various voxel, element and pore size

	Tension	voxel size	FE-size	d ₅₀	MOR	ε(MOR)
	Mat #	um	um	um	GPa	
R1 120 ³	4	6.72	1.12	22	0.268	0.359
	5	6.72	1.34	22	0.269	0.396
	6	6.72	1.68	22	0.266	0.392
	7	6.72	2.24	22	0.265	0.413
	8	6.72	3.36	22	0.259	0.384
	9	6.72	6.72	22	0.255	0.356
R1, quarter	7	6.72	2.24	22	0.132	0.210
	8	6.72	3.36	22	0.137	0.218
	9	6.72	6.72	22	0.136	0.210
Virtual structures	p = 0.3					
	1	1.00	1.00	5.5	0.861	0.540
	11	2.00	2.00	5.5	0.784	0.490
	p = 0.4					
	1	3.00	1.00	5.5	0.480	0.495
	2	3.00	1.50	5.5	0.485	0.448
	3	3.00	3.00	5.5	0.492	0.446
	p = 0.5					
	1	3.00	1.00	5.5	0.383	0.625
	2	3.00	1.50	5.5	0.379	0.558
	3	3.00	3.00	5.5	0.392	0.519
	p = 0.6					
	1	3.00	1.00	5.5	0.196	0.549
	2	3.00	1.50	5.5	0.216	0.602
	3	3.00	3.00	5.5	0.259	0.579

Table 4. Compressive strength and strain tolerance

	Compression	voxel size	FE-size	d ₅₀	MOR, GPa	ε(MOR)
	Mat #	um	um	um	GPa	
R1 120 ³	4	6.72	1.12	22	-0.72	-0.973
	5	6.72	1.34	22	-0.74	-0.988
	6	6.72	1.68	22	-0.70	-0.934
	7	6.72	2.24	22	-0.68	-0.881
	8	6.72	3.36	22	-0.64	-0.845
	9	6.72	6.72	22	-0.61	-0.770
R1, quarter	7	6.72	2.24	22	-0.43	-0.757
	8	6.72	3.36	22	-0.43	-0.706
	9	6.72	6.72	22	-0.44	-0.639
Virtual structures	p = 0.3					
	1	1.00	1.00	5.5	-2.87	-1.800
	11	2.00	2.00	5.5	-2.59	-1.670
	p = 0.4					
	1	3.00	1.00	5.5	-1.52	-0.156
	2	3.00	1.50	5.5	-1.52	-0.150
	3	3.00	3.00	5.5	-1.62	-0.157
	p = 0.5					
	1	3.00	1.00	5.5	-1.02	-0.164
	2	3.00	1.50	5.5	-1.13	-0.174
	3	3.00	3.00	5.5	-1.23	-0.162
	p = 0.6					
	1	3.00	1.00	5.5	-0.50	-0.151
	2	3.00	1.50	5.5	-0.62	-0.166
	3	3.00	3.00	5.5	-0.74	-0.178

Table 5. Summary of calculated mechanical parameters for synthetic structures (input Material #12)

Overlapping pores	m	MOR ^{compr} , GPa	MOR ^{tens} , GPa	MOR ^{compr} /MOR ^{tens}
p = 0.30	2.04	11.85	3.55	3.34
p = 0.40	1.98	8.19	2.42	3.38
p = 0.50	2.00	5.93	1.86	3.19
p = 0.60	2.07	3.71	1.29	2.88
Overlapping solids				
p = 0.41	3.41	3.01	0.98	3.07
p = 0.52	3.95	0.95	0.38	2.50
p = 0.63	4.24	0.25	0.09	2.78

Table 6. Calculated average strength (GPa) and statistical deviations (in brackets)

Average strength, GPa	Tension	Compression
Overlapping spherical pores	7.5 (11%)	23.9 (4%)
Overlapping spherical solids	6.3 (8%)	17.5 (4%)

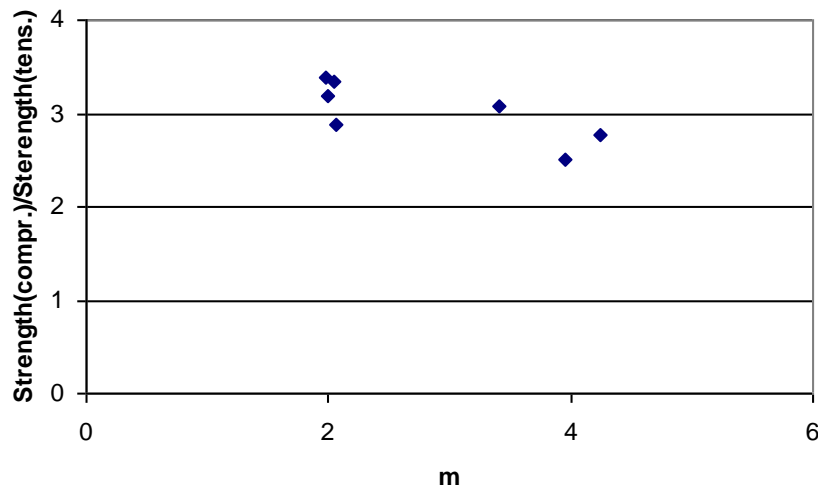


Figure 25. Compressive/Tensile strength ratio as function of pore morphology

Conclusions

1. A number of FEM simulations on virtually generated and real tomography 3D pore structures has been performed to search for a feasible way to numerically study the influence of pore structure on mechanical strength of ceramics structures

2. It has been shown that the approach of element deletion may give reasonable numerical estimates of specific structure strength when a proper element deletion criterion is used.

3. An element failure criterion has been developed to address the calculated strength dependence on the finite element size. The criterion worked reasonably well for the samples considered and can be recommended for usage in comparative simulations of complex 3D structure failures at various load modes and meshes.

4. A previous conclusion [24] has been confirmed for the tomography resolution required to adequately simulate porous structures in 3D. With the resolution being finer than the median pore size $V < D50_{min}$, one should obtain consistent results suitable for comparative analyses. It could be noted that the samples of overlapping spherical pores/overlapping spherical solids are representative when their linear dimensions are 8-10 larger than their median pore size d_{50} . Natural structures with irregularly shaped pores should require larger relative sample sizes to produce stable mechanical property calculation or experimental results.

References

1. Krivoshapkina Ye.F., Krivoshapkin P.V., Dudkin B.N. Mikroporistaya keramika kordiyeritovogo sostava na osnove prirodnogo syrya [Microporous cordierite ceramics on a natural raw material]. *Izvestiya Komi nauchnogo tsentra UrO RAN*. 2011. No. 7. Pp. 27–32. (rus)
2. Solovyev S.A. Okislitel'naya konversiya metana na strukturirovannykh katalizatorakh Ni–Al₂O₃/Kordierit [Oxidative methane conversion on structural catalysts Ni–Al₂O₃/Cordierite]. *Catalysis in Industry*. 2011. No. 4. Pp. 31–42. (rus)
3. Gassmann F. Uber Die elastizitat poroser medien. *Vier der Natur Gesellschaft*. 1951. No. 96. Pp. 1–23.
4. Kachanov M., Tsukrov I., Shafiro B. Effective Moduli of Solids With Cavities of Various Shapes. *Applied Mechanics Reviews*. 1994. Vol. 47(1S). Pp. 151–174.
5. Kachanov M., Sevostianov I., Shafiro B. Explicit cross-property correlations for porous materials with anisotropic microstructures. *Journal of the Mechanics and Physics of Solids*. 2001. Vol. 49(1). Pp. 1–25.
6. Knudsen F.P. Dependence of Mechanical Strength of Brittle Polycrystalline Specimens on Porosity and Grain Size. *Journal of the American Ceramic Society Volume*. 1959. Vol. 42(8). Pp. 376–387.
7. Bruno G., Efremov A.M., Levandovskiy A.N., Clausen B.

Литература

1. Кривошапкина Е.Ф., Кривошапкин П.В., Дудкин Б.Н. Микропористая керамика кордиеритового состава на основе природного сырья. // Известия Коми научного центра УрО РАН. 2011. № 7. С. 27–32.
2. Соловьев С.А. Окислительная конверсия метана на структурированных катализаторах Ni–Al₂O₃/Кордиерит // Катализ в промышленности. 2011. № 4. С. 31–42.
3. Gassmann F. Uber Die elastizitat poroser medien // Vier der Natur Gesellschaft. 1951. № 96. Pp. 1–23.
4. Kachanov M., Tsukrov I., Shafiro B. Effective moduli of solids with cavities of various shapes // Applied Mechanics Reviews. 1994. Vol. 47(1S). Pp. 151–174.
5. Kachanov M., Sevostianov I., Shafiro B. Explicit cross-property correlations for porous materials with anisotropic microstructures // Journal of the Mechanics and Physics of Solids. 2001. Vol. 49(1). Pp. 1–25.
6. Knudsen F.P. Dependence of Mechanical Strength of Brittle Polycrystalline Specimens on Porosity and Grain Size // Journal of the American Ceramic Society Volume. 1959. Vol. 42(8). Pp. 376–387.
7. Bruno G., Efremov A.M., Levandovskiy A.N., Clausen B. Connecting the macro- and microstrain responses in technical porous ceramics: modeling and experimental validations // Journal of Materials Science. 2011. Vol. 46(1).

Левандовский А.Н., Мельников Б.Е., Шамкин А.А. Моделирование разрушения пористого материала // Инженерно-строительный журнал. 2017. № 1(69). С. 3–22.

- Connecting the macro- and microstrain responses in technical porous ceramics: modeling and experimental validations. *Journal of Materials Science*. 2011. Vol. 46(1). Pp. 161–173.
8. Roberts A., Garboczi E.J. Elastic properties of model porous ceramics. *Journal of the American Ceramic Society*. 2000. Vol. 83(12). Pp. 3041–3048.
 9. Shmitko Ye.I., Rezanov A.A., Bedarev A.A. Multiparametricheskaya optimizatsiya struktury yacheistogo silikatnogo betona [Multi-parametric optimization of the silicate cell concrete structure]. *Magazine of Civil Engineering*. 2013. No. 3. Pp. 15–23. (rus)
 10. Courant R. Variational methods for the solution of problems of equilibrium and vibrations. *Bulletin of American Mathematic Society*. 1943. Vol. 49. Pp. 1–23.
 11. Galerkin B.G. *Sobraniye sochineniy* [Collected works]. Vol. I. M.: Izdatelstvo AN SSSR, 1952. 391 p. (rus)
 12. Timoshenko S.P., Voynovskiy-Kriger S. *Plastiny i obolochki* [Plates and shells]. M.: Nauka, 1966. 635 p. (rus)
 13. Rozin L.A. *Sterzhnevyye sistemy kak sistemy konechnykh elementov* [Beam systems as systems of finite elements]. L.: Izd-vo LGU, 1976. 232 p. (rus)
 14. Asheychik A.A., Polonskiy V.L. *Raschet detaley mashin metodom konechnykh elementov* [Machinery details processing by the finite element method]. SPb.: Izd-vo SPbGPU, 2016. 243 p. (rus)
 15. Roberts A.P., Garboczi E.J. Elastic properties of model random three-dimensional open-cell solids. *Journal of the Mechanics and Physics of Solids*. 2002. Vol. 50(1). Pp. 33–55.
 16. Roberts A., Garboczi E.J. Computation of the linear elastic properties of random porous materials with a wide variety of microstructure. *Proceedings of the Royal Society. Series A: Mathematical, Physical and Engineering Sciences*. 2002. Vol. 458(2021). Pp. 1033–1054.
 17. Charles P. Ursebach Simulation of elastic moduli for porous materials. *CREWES Research Report*. 2001. Vol. 13. Pp. 83–98.
 18. Bauer J.S., Sidorenko I., Mueller D., Baum T. Prediction of bone strength by μ CT and MDCT-based finite-element-models: How much spatial resolution is needed? *European Journal of Radiology*. 2014. Vol. 83(1). Pp. 36–42.
 19. Shtern M.B., Kuzmov A.V., Frolova Ye.G., Vdovichenko A.V. Issledovaniye uprugogo povedeniya poroshkovykh materialov s ploskimi porami metodom pryamogo kompyuternogo modelirovaniya na elementarnoy yacheyke [Study of the elastic behavior of the powder materials with flat pores by direct computer modeling on an elementary cell]. *Naukovi notatki Zbirnik naukovikh prats*. 2005. No. 17. Pp. 390–398. (rus)
 20. Garboczi E.J., Day A.R. An algorithm for computing the effective linear elastic properties of heterogeneous materials: 3D results for composites with equal phase Poisson ratios. *Journal of the Mechanics and Physics of Solids*. 1995. Vol. 43. Pp. 1349–1362.
 21. Razina I.S., Semenova S.G., Sattarov A.G., Musin I.N. Primeneniye mikrotomografii dlya issledovaniya novykh materialov. Obzor [Micro tomography use for new materials study. A review]. *Vestnik Kazanskogo gosudarstvennogo tekhnologicheskogo universiteta. Kazan: Izd-vo Kazanskogo gosudarstvennogo tekhnologicheskogo universiteta*. 2013. Vol. 16. No. 19. Pp. 163–169. (rus)
 22. Garboczi E.J. Bentz D.P., Martys N.S. *Digital images and computer modeling in "Methods of the Physics of Porous Media"*. Ed. P.-z. Wong. San Diego: Academic Press, 1999. Vol. 35(1). Pp. 1–41.
 23. Garboczi E.J. *Finite element and finite difference programs for computing the linear electric and elastic properties of digital images of random materials* [Elektronnyy resurs] Sistem. trebovaniya: Adobe Acrobat Reader. URL: ftp://ftp.nist.gov/pub/bfrl/garbocz/DFEMANUAL/MANUAL.pdf (дата обращения: 20.11.2016)
 24. Levandovskiy A., Melnikov B. Finite element modeling of porous material structure represented by a uniform cubic mesh // *Applied Mechanics and Materials*. 2015. Vol. 725–726. Pp. 928–936.
 25. Levandovskiy A.N., Efremov A.M., Bruno G. Macro to micro stress and strain conversion in porous ceramics // *Materials*. Pp. 161–173.
 8. Roberts A., Garboczi E.J. Elastic properties of model porous ceramics // *Journal of the American Ceramic Society*. 2000. Vol. 83(12). Pp. 3041–3048.
 9. Шмитко Е.И., Резанов А.А., Бедарев А.А. Мультипараметрическая оптимизация структуры ячеистого силикатного бетона // *Инженерно-строительный журнал*. 2013. № 3. С. 15–23.
 10. Courant R. Variational methods for the solution of problems of equilibrium and vibrations // *Bulletin of American Mathematic Society*. 1943. Vol. 49. Pp. 1–23.
 11. Галеркин Б.Г. *Собрание сочинений*. Том I. М.: Издательство АН СССР, 1952. 391 с.
 12. Тимошенко С.П., Войновский-Кригер С. *Пластины и оболочки*. М.: Наука, 1966. 635 с.
 13. Розин Л.А. *Стержневые системы как системы конечных элементов*. Л.: Изд-во ЛГУ, 1976. 232 с.
 14. Ашейчик А.А., Полонский В.Л. *Расчёт деталей машин методом конечных элементов*. СПб.: Изд-во СПбГПУ, 2016. 243 с.
 15. Roberts A.P., Garboczi E.J. Elastic properties of model random three-dimensional open-cell solids // *Journal of the Mechanics and Physics of Solids*. 2002. Vol. 50(1). Pp. 33–55.
 16. Roberts A., Garboczi E.J. Computation of the linear elastic properties of random porous materials with a wide variety of microstructure // *Proceedings of the Royal Society. Series A: Mathematical, Physical and Engineering Sciences*. 2002. Vol. 458(2021). Pp. 1033–1054.
 17. Charles P. Ursebach Simulation of elastic moduli for porous materials // *CREWES Research Report*. 2001. Vol. 13. Pp. 83–98.
 18. Bauer J.S., Sidorenko I., Mueller D., Baum T. Prediction of bone strength by μ CT and MDCT-based finite-element-models: How much spatial resolution is needed? // *European journal of radiology*. 2014. Vol. 83(1). Pp. 36–42.
 19. Штерн М.Б., Кузьмов А.В., Фролова Е.Г., Вдовиченко А.В. *Исследование упругого поведения порошковых материалов с плоскими порами методом прямого компьютерного моделирования на элементарной ячейке* // *Наукові нотатки Збірник наукових праць*. 2005. № 17. С. 390–398.
 20. Garboczi E.J., Day A.R. An algorithm for computing the effective linear elastic properties of heterogeneous materials: 3D results for composites with equal phase Poisson ratios // *Journal of the Mechanics and Physics of Solids*. 1995. Vol. 43. Pp. 1349–1362.
 21. Разина И.С., Семенова С.Г., Саттаров А.Г., Мусин И.Н. *Применение микротомографии для исследования новых материалов. Обзор* // *Вестник Казанского государственного технологического университета*. Казань: Изд-во Казанского государственного технологического университета; 2013. Т. 16. № 19. С. 163–169.
 22. Garboczi E.J. Bentz D.P., Martys N.S. *Digital images and computer modeling in "Methods of the Physics of Porous Media"* // San Diego: Academic Press, 1999. Vol. 35(1). Pp. 1–41.
 23. Garboczi E.J. *Finite element and finite difference programs for computing the linear electric and elastic properties of digital images of random materials* [Электронный ресурс] Систем. требования: Adobe Acrobat Reader. URL: ftp://ftp.nist.gov/pub/bfrl/garbocz/DFEMANUAL/MANUAL.pdf (дата обращения: 20.11.2016)
 24. Levandovskiy A., Melnikov B. Finite element modeling of porous material structure represented by a uniform cubic mesh // *Applied Mechanics and Materials*. 2015. Vol. 725–726. Pp. 928–936.
 25. Levandovskiy A.N., Efremov A.M., Bruno G. Macro to micro stress and strain conversion in porous ceramics // *Materials*

Levandovskiy A.N., Melnikov B.E., Shamkin A.A. Modeling of porous material fracture. *Magazine of Civil Engineering*. 2017. No. 1. Pp. 3–22. doi: 10.18720/MCE.69.1

- (data obrashcheniya: 20.11.2016)
24. Levandovskiy A., Melnikov B. Finite element modeling of porous material structure represented by a uniform cubic mesh. *Applied Mechanics and Materials*. 2015. Vol. 725–726. Pp. 928–936.
 25. Levandovskiy A.N., Efremov A.M., Bruno G. Macro to micro stress and strain conversion in porous ceramics. *Materials Science Forum*. 2012. Vol. 706–709. Pp. 1667–672.
 26. Huang Y., Yang Z., Ren W., Liu G. 3D meso-scale fracture modelling and validation of concrete based on in-situ X-ray computed tomography images using damage plasticity model. *International Journal of Solids and Structures*. 2015. Vol. 67. Pp. 340–352.
 27. Emerson J.E., Matt J.C., Reilly G.C., Amaka C. Offiah Geometrically accurate 3D FE models from medical scans created to analyze the causes of sports injuries. *Procedia Engineering*. 2011. Vol. 13. Pp. 422–427.
 28. Roshchin P.V., Rogachev M.K., Vaskes Kardenas L.K., Kuzmin M.I., Litvin V.T., Zinov'ev A.M. Issledovaniye kernovogo materiala Pecherskogo mestorozhdeniya prirodnogo bituma s pomoshchyu rentgenovskogo kompyuternogo mikrotomografa SKYSCAN 1174V2 [Kern material study of the Pecherski field with the computer micro tomograph SKYSCAN 1174 v2]. *Mezhdunarodnyy nauchno-issledovatel'skiy zhurnal*. 2013. No. 8(15). Part 2. Pp. 45–48. (rus)
 29. Yiotis A.G., Kainourgiakis M.E., Eustathios S. Kikkinides, Stubos A.K. Application of the Lattice-Boltzmann method to the modeling of population blob dynamics in 2 D porous domains. *Computers & Mathematics with Applications*. 2010. Vol. 59(7). Pp. 2315–2325.
 30. Mo L.T., Huurman M., Wu S.P., Molenaar A.A.A. 2D and 3D meso-scale finite element models for ravelling analysis of porous asphalt concrete. *Finite Elements in Analysis and Design*. 2008. Vol. 44(4). Pp. 186–196.
 31. Gorshkov A.S., Vatin N.I. Svoystva stenovykh konstruktсий iz yacheistobetonnykh izdeliy avtoklavnogo tverdeniya na poliuretановом kleу [Wall structures properties made of cell concrete on polyurethane glues]. *Magazine of Civil Engineering*. 2013. No. 5. Pp. 5–19. (rus)
 32. Gorshkov A.S., Vatin N.I. Innovatsionnaya tekhnologiya vozvedeniya stenovykh konstruktсий iz gazobetonnykh blokov na poliuretановyy kleу [Wall structures properties made of cell concrete on polyurethane glues]. *Construction of Unique Buildings and Structures*. 2013. No. 8. Pp. 20–28. (rus)
 33. Nikitin A.N., Ivankina T.I., Sobolev G.A., Sheftsyuk K., Frishbutter A., Valter K. Neytronograficheskiye issledovaniya vnutrikristallicheskiy deformatsiy i napryazheniy v obraztse mramora pri povyshennykh temperaturakh i vnesnykh mekhanicheskikh nagruzkakh [Neutron studies of the crystal deformations and stresses in marble under high temperature and mechanical loading]. *Izvestia. Physics of the Solid Earth*. M.: Nauka, 2004. No. 1. Pp. 88–92. (rus)
 34. Frishbutter A., Neov D., Scheffzuk C., Vrana M., Walther K. Lattice strain measurements on sandstones under load using neutron diffraction. *Journal of Structural Geology*. 2000. Vol. 22(11–12). Pp. 1587–1600.
 35. Darling T.W., TenCate J.A., Brown D.W., Clausen B., Vogel S.C. Neutron diffraction study of the contribution of grain contacts to nonlinear stress-strain behavior. *Geophysical Research Letters*. 2004. Vol. 31(16/L16604). Pp. 1–4.
 36. *Electronic source: CeramTec GmbH* [Electronic source]. URL: <https://www.ceramtec.com/alutit/> (date: 01.02.2017).
 37. Bruno G., Efremov A.M., Levandovskiy A.N., Pozdnyakova I., Hughes D.J., Clausen B. Thermal and mechanical response of industrial porous ceramics. *Materials Science Forum*. 2010. Vol. 652. Pp. 191–196.
 38. Kouznetsova V.G. *Computational homogenization for the multi-scale analysis of multi-phase materials*: doctoral dissertation: 9.12.02. Kouznetsova Varvara. Eindhoven, 2002. 134 p.
 39. Bubeck C. Direction dependent mechanical properties of extruded cordierite honeycombs // *Journal of the European Ceramic Society*. 2009. Vol. 29(15). Pp. 3113–3119.
 40. Wereszczak A., Fox E., Lance M., Ferber M. Failure stress and apparent elastic modulus of diesel particulate filter ceramics // *SAE International Journal of Materials and Manufacturing*. 2012. Vol. 5(2012-01-1252). Pp. 517–527.
 41. Boger T., Tilgner I.C., Shen M., Jiang Y. Oxide based particulate filters for light-duty diesel applications – impact of the filter length on the regeneration and pressure drop // *Science Forum*. 2012. Vol. 706–709. Pp. 1667–672.
 42. Huang Y., Yang Z., Ren W., Liu G. 3D meso-scale fracture modelling and validation of concrete based on in-situ X-ray computed tomography images using damage plasticity model // *International Journal of Solids and Structures*. 2015. Vol. 67. Pp. 340–352.
 43. Emerson J.E., Matt J.C., Reilly G.C., Amaka C. Offiah Geometrically accurate 3D FE models from medical scans created to analyze the causes of sports injuries // *Procedia Engineering*. 2011. Vol. 13. Pp. 422–427.
 44. Рощин П.В., Рогачев М.К., Васкес Карденас Л.К., Кузьмин М.И., Литвин В.Т., Зиновьев А.М. Исследование кернового материала Печерского месторождения природного битума с помощью рентгеновского компьютерного микротомографа SKYSCAN 1174V2 // *Международный научно-исследовательский журнал*. 2013. № 8(15). Ч. 2. С. 45–48.
 45. Yiotis A.G., Kainourgiakis M.E., Eustathios S. Kikkinides, Stubos A.K. Application of the Lattice-Boltzmann method to the modeling of population blob dynamics in 2 D porous domains. // *Computers & Mathematics with Applications*. 2010. Vol. 59(7). Pp. 2315–2325.
 46. Mo L.T., Huurman M., Wu S.P., Molenaar A.A.A. 2D and 3D meso-scale finite element models for ravelling analysis of porous asphalt concrete // *Finite Elements in Analysis and Design*. 2008. Vol. 44(4). Pp. 186–196.
 47. Горшков А.С., Ватин Н.И. Свойства стеновых конструкций из ячеистобетонных изделий автоклавного твердения на полиуретановом клею // *Инженерно-строительный журнал*. 2013. № 5. С. 5–19.
 48. Горшков А.С., Ватин Н.И. Инновационная технология возведения стеновых конструкций из газобетонных блоков на полиуретановый клей // *Строительство уникальных зданий и сооружений*. 2013. № 8. С. 20–28.
 49. Никитин А.Н., Иванкина Т.И., Соболев Г.А., Шефцук К., Фришбюттер А., Вальтер К. Нейтронграфические исследования внутрикристаллических деформаций и напряжений в образце мрамора при повышенных температурах и внешних механических нагрузках // *Физика Земли*. М.: Наука, 2004. № 1. С. 88–92.
 50. Frishbutter A., Neov D., Scheffzuk C., Vrana M., Walther K. Lattice strain measurements on sandstones under load using neutron diffraction // *Journal of Structural Geology*. 2000. Vol. 22(11–12). Pp. 1587–1600.
 51. Darling T.W., TenCate J.A., Brown D.W., Clausen B., Vogel S.C. Neutron diffraction study of the contribution of grain contacts to nonlinear stress-strain behavior // *Geophysical Research Letters*. August 2004. Vol. 31(16/L16604). Pp. 1–4.
 52. Электронный источник: CeramTec GmbH [Электронный ресурс]. Систем. требования: IE. URL: <https://www.ceramtec.com/alutit/> (дата обращения: 01.02.2017).
 53. Bruno G., Efremov A.M., Levandovskiy A.N., Pozdnyakova I., Hughes D.J., Clausen B. Thermal and mechanical response of industrial porous ceramics // *Materials Science Forum*. 2010. Vol. 652. Pp. 191–196.
 54. Kouznetsova V.G. *Computational homogenization for the multi-scale analysis of multi-phase materials*: doctoral dissertation: 9.12.02. Kouznetsova Varvara. Eindhoven, 2002. 134 p.
 55. Bubeck C. Direction dependent mechanical properties of extruded cordierite honeycombs // *Journal of the European Ceramic Society*. 2009. Vol. 29(15). Pp. 3113–3119.
 56. Wereszczak A., Fox E., Lance M., Ferber M. Failure stress and apparent elastic modulus of diesel particulate filter ceramics // *SAE International Journal of Materials and Manufacturing*. 2012. Vol. 5(2012-01-1252). Pp. 517–527.
 57. Boger T., Tilgner I.C., Shen M., Jiang Y. Oxide based particulate filters for light-duty diesel applications – impact of the filter length on the regeneration and pressure drop // *Science Forum*. 2012. Vol. 706–709. Pp. 1667–672.
- Левандовский А.Н., Мельников Б.Е., Шамкин А.А. Моделирование разрушения пористого материала // *Инженерно-строительный журнал*. 2017. № 1(69). С. 3–22.

2002. 134 p.
39. Bubeck C. Direction dependent mechanical properties of extruded cordierite honeycombs. *Journal of the European Ceramic Society*. 2009. Vol. 29(15). Pp. 3113–3119.
40. Wereszczak A., Fox E., Lance M., Ferber M. Failure stress and apparent elastic modulus of diesel particulate filter ceramics. *SAE International Journal of Materials and Manufacturing*. 2012. Vol. 5(2012-01-1252). Pp. 517–527.
41. Boger T., Tilgner I.C., Shen M., Jiang Y. Oxide based particulate filters for light-duty diesel applications – impact of the filter length on the regeneration and pressure drop behavior. *SAE International Journal of Fuels and Lubricants*. 2008. Vol. 1(2008-01-0485). Pp. 252–264.
42. Ingram-Ogunwumi R.S., Dong Q., Murrin T.A., Bhargava R.Y., Warkins J.L., Heibel A.K. Performance evaluations of aluminum titanate diesel particulate filters. *SAE Technical Paper*. 2007. No. 2007-01-0656.
43. Williams M.L. Stress singularities resulting from various boundary conditions in angular corner plates in extension. *Journal of Applied Mechanics*. 1952. Vol. 19. Pp. 526–528.
- behavior // *SAE International Journal of Fuels and Lubricants*. 2008. Vol. 1(2008-01-0485). Pp. 252–264.
42. Ingram-Ogunwumi R.S., Dong Q., Murrin T.A., Bhargava R.Y., Warkins J.L., Heibel A.K. Performance evaluations of aluminum titanate diesel particulate filters // *SAE Technical Paper*. 2007. No. 2007-01-0656.
43. Williams M.L. Stress singularities resulting from various boundary conditions in angular corner plates in extension // *Journal of Applied Mechanics*. 1952. Vol. 19. Pp. 526–528.

Andrey Levandovskiy,
+7(904)5157287; levandovan@corning.com

Boris Melnikov,
+7(812)5526303; kafedra@ksm.spbstu.ru

Artemiy Shamkin,
+7(911)7366391; shamkinaa@corning.com

Андрей Николаевич Левандовский,
+7(904)5157287;
эл. почта: levandovan@corning.com

Борис Евгеньевич Мельников,
+7(812)5526303;
эл. почта: kafedra@ksm.spbstu.ru

Артеми́й Александрович Шамкин,
+7(911)7366391;
эл. почта: shamkinaa@corning.com

© Levandovskiy A.N., Melnikov B.E., Shamkin A.A., 2017